

Article

Trace Elements and Pb-O Isotopes of Scheelite: Metallogenic Implications for the Shimensi W-Polymetallic Deposit in South China

Peng Wang^{1,2}, Ting Liang^{1,*}, HongJun Jiang², XinKui Xiang³ and Bo Zhong³¹ School of Earth Science and Resources, Chang'an University, Xi'an 710054, China² Geological Party No. 214, Sino Shaanxi Nuclear Industry Group, Xi'an 710100, China³ No. 916 Geological Team of Jiangxi Geology & Mineral Exploration Bureau, Jiujiang 332100, China

* Correspondence: liangt@chd.edu.cn

Abstract: The world-class Shimensi tungsten (W)-polymetallic deposit is located in Jiangnan Orogen, with an estimated reserve of 742.5 kt WO₃ @ 0.195% W, 403.6 kt Cu and 28 kt Mo. In this paper, the trace elements and Pb-O isotopes of scheelite (the main ore mineral) are presented to study the ore-forming material source and ore-forming fluid evolution. The results show that the REE distribution in scheelite is mainly controlled by the substitution mechanism of $3Ca^{2+} = 2REE^{3+} + \square Ca$ (where $\square Ca$ is the Ca-site vacancy). Oxygen isotope data indicate that the scheelite mineralization occurred under high-temperature oxygen isotope equilibrium conditions, and that the ore-forming fluid has a magmatic-hydrothermal origin. The variation in scheelite Eu anomalies and the wide range of scheelite Y/Ho ratio indicate that the ore-forming fluid evolves from reducing to oxidizing, and the early-stage and late-stage ore-forming fluid may have been relatively rich in F⁻ and HCO₃⁻, respectively. The significant Mo decrease in scheelite from the early to late stage that are opposite to the influence of fO_2 variation may have resulted from the crystallization of molybdenite and Mo-rich scheelite. Lead isotopes of the ore minerals of scheelite, wolframite, molybdenite and chalcopyrite can be divided into three groups, similar to these of feldspars in different granites. Both the Mesozoic porphyritic and fine-grained biotite granites have Pb isotope ratios similar to the ores, which suggests that the former two are the main ore material source.

Keywords: scheelite; trace and REE elements; Pb isotopes; O isotopes; Shimensi W deposit

Citation: Wang, P.; Liang, T.; Jiang, H.; Xiang, X.; Zhong, B. Trace Elements and Pb-O Isotopes of Scheelite: Metallogenic Implications for the Shimensi W-Polymetallic Deposit in South China. *Minerals* **2022**, *12*, 1461. <https://doi.org/10.3390/min12111461>

Academic Editor: Maria Boni

Received: 29 September 2022

Accepted: 8 November 2022

Published: 18 November 2022

Publisher's Note: MDPI stays neutral with regard to jurisdictional claims in published maps and institutional affiliations.



Copyright: © 2022 by the authors. Licensee MDPI, Basel, Switzerland. This article is an open access article distributed under the terms and conditions of the Creative Commons Attribution (CC BY) license (<https://creativecommons.org/licenses/by/4.0/>).

1. Introduction

Several giant granite intrusion-related tungsten deposits, including the Dahutang and Zhuxi [1–4], have been discovered in northern Jiangxi Province (South China). The Shimensi W deposit is an important part of the Dahutang ore field. Previous studies have focused on the deposit geology, ore-forming age, ore-forming fluid and geochemical features of ore-related granites [1,5–18]. Moreover, Sun and Chen [19] and Chen et al. [20] reported the scheelite elemental data of veinlet-disseminated and quartz-vein mineralization types, respectively. These works play an important role in aiding our understanding of the Shimensi ore-forming genesis. The evolution process of different ore stages and the origin of ore-forming metals remain a controversial topic in the literature. In this study, the trace elements of scheelite and the Pb and O isotope signatures of the minerals in the Shimensi deposit were analyzed, attempting to provide a better understanding of the metallogenic material sources and ore-forming nature of the Shimensi deposit.

2. Regional Geological Background

The Shimensi W deposit is located in the central area of Jiangnan Orogen, which is located between the Yangtze and Cathaysia Craton (Figure 1) [21]. The NE-trending Jiangnan Orogen (ca. 1500 km long), a significant tectonic-magmatic-metallogenic belt

located in south China, has experienced complex tectonic evolution, including the Neoproterozoic orogeny, Paleozoic depression and Mesozoic strong compressional uplift [22]. It is mainly composed of Neoproterozoic metasedimentary rocks and granites with minor mafic rocks [23–26]. The lower part of metasedimentary sequence is the Shuangqiaoshan Group, which can be subdivided further (from oldest to youngest) into the Hengyong, Jilin, Anlelin and Xiushui Formations [27,28]. The Shuangqiaoshan Group, overlain across an unconformity by the Dengshan Group [29], mainly consists of tuffaceous sandstone and phyllite-slate, and minor spilite and quartz-keratophyre, with depositional ages ranging from 860 Ma to 825 Ma [28,30]. The average W content in the strata is 9.13 ppm, which is 3.23 times higher than the crust Clarke value [15,30,31].

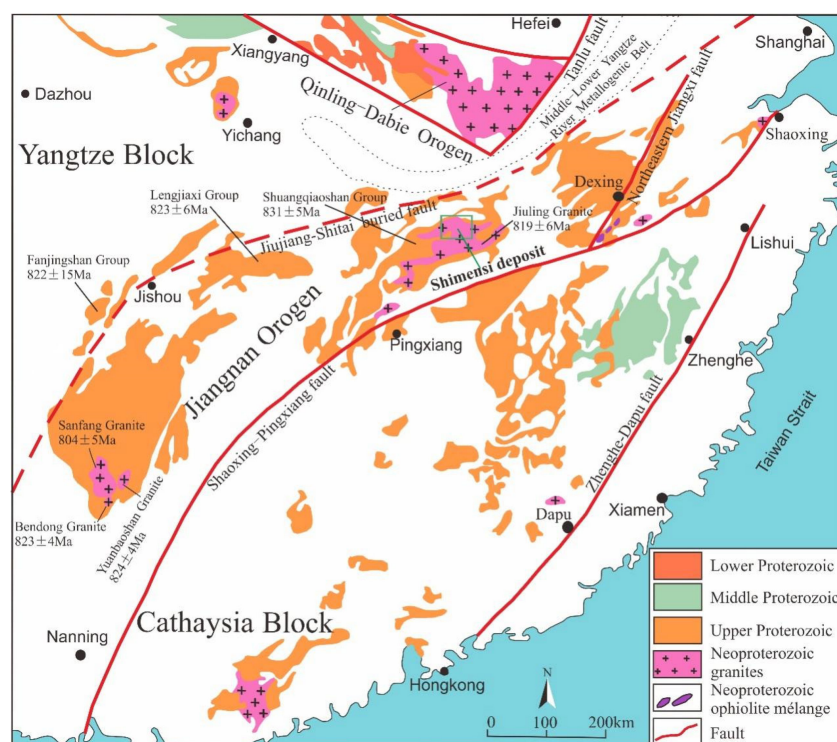


Figure 1. Map presenting the distribution of granites and volcanic rocks in south China, and also the location of the Jiangnan Orogen and the Shimensi ore deposit (modified after [21]).

Neoproterozoic and Mesozoic granitic rocks are well-developed in the area. The Neoproterozoic biotite granodiorite, distributed approximately E–W-trending, is part of the Jiuling granodiorite batholith, the largest granitoid complex in SE China (outcrop size >2500 km²) [32]. The batholite granodiorite was zircon LA-ICP-MS and SHRIMP U-Pb dated to be ca. 820 Ma [11,14,32,33] and intruded the Shuangqiaoshan Group. It is peraluminous and characterized by high CaO/Na₂O, and low Rb/Sr and Rb/Ba ratios, and has Sr-Nd isotopes similar to those of the Shuangqiaoshan Group [33]. The Mesozoic granitic rocks, predominately consisting of porphyritic biotite granite, fine-grained biotite granite and granite porphyry, intruded in both the Neoproterozoic biotite granodiorite and Shuangqiaoshan Group, and show a close relationship with the W mineralization [7–10,34]. The overall NE–ENE-trending faults cut the Neoproterozoic strata and biotite granodiorite, and controlled the distribution of both granite emplacement and W-polymetallic mineralization. A total of 15 W-polymetallic deposits are present in the ore field (size: 20 × 10 km), among which five are medium to (super-)large in size, i.e., the Shimensi, Dongdouya, Dalingshang, Shiweidong and Kunshan (Figure 2).

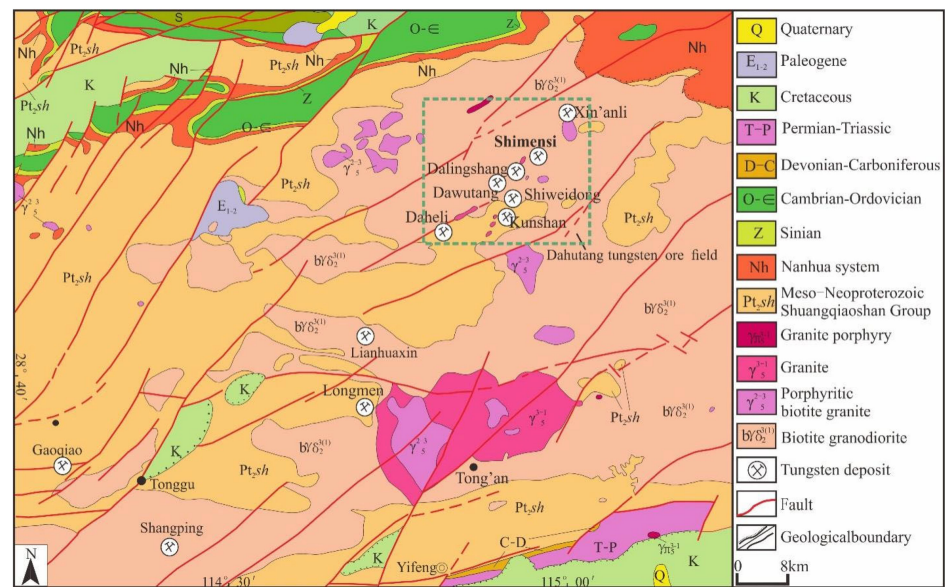


Figure 2. Geological and mineral map of the Jiulingshan region (modified after [16]).

3. Deposit Geology

Large-scale Neoproterozoic and Mesozoic magmatism occurred in the Shimensi mining area, with minor Quaternary overburden sediments (Figure 3). The grayish Neoproterozoic coarse-grained biotite granodiorite covers 80% of the deposit area, and contains 30–35% quartz, 27–35% plagioclase, 10–15% potassic feldspar, 5–10% biotite and accessory (<5%) muscovite and cordierite [33]. The Mesozoic granites include porphyritic biotite granite (ca. 148.3–147.4 Ma), fine-grained biotite granite (ca. 146.1–144.7 Ma) and granite porphyry (ca. 143.1–143.0 Ma) [10,34]. The porphyritic biotite granite, distributed in central Shimensi, intruded in the Neoproterozoic granodiorite batholith in the forms of sills and dykes. The fine-grained biotite granite, distributed in southeastern Shimensi as sills, cut both the porphyritic biotite granite and Neoproterozoic biotite granodiorite. The granite porphyry occurs in central Shimensi as narrow dykes and cut other granitoids. All of these three granites feature high-Si, peraluminous, high-K and calc-alkaline granites, and belong to the S-type granite [22]. The W mineralization mainly occurs in Neoproterozoic biotite granodiorite and Mesozoic porphyritic biotite granite. Considering that the former has a higher CaO content than the latter and there are no carbonate sequences present in the area, the Neoproterozoic biotite granodiorite is suggested to provide Ca to the scheelite (CaWO₄) orebodies [22,33]. Scheelite mineralization can also be observed in the fine-grained granite, whereas chalcopyrite mineralization occurs in the granite porphyry [33]. There is also a 0.5–1.5 m thick pegmatite zone with K-feldspar megacrysts that has developed along the contact zone between the Neoproterozoic biotite granodiorite and Mesozoic porphyritic biotite granite. Local structures include ductile shear zones, faults and joints, and trend NNE to ENE and NW, which has been interpreted to have formed by Neoproterozoic and Mesozoic tectonic movements [16]. Feng et al. [1] reported a molybdenite Re-Os age of 143.7 ± 1.2 Ma for the Shimensi mineralization, which is consistent with the scheelite Sm-Nd age (142.4 ± 8.9 Ma) reported by Huang [35], suggesting that the Shimensi W mineralization occurred in the Early Cretaceous and is likely associated with the Mesozoic granites, especially porphyritic biotite and fine-grained granites.

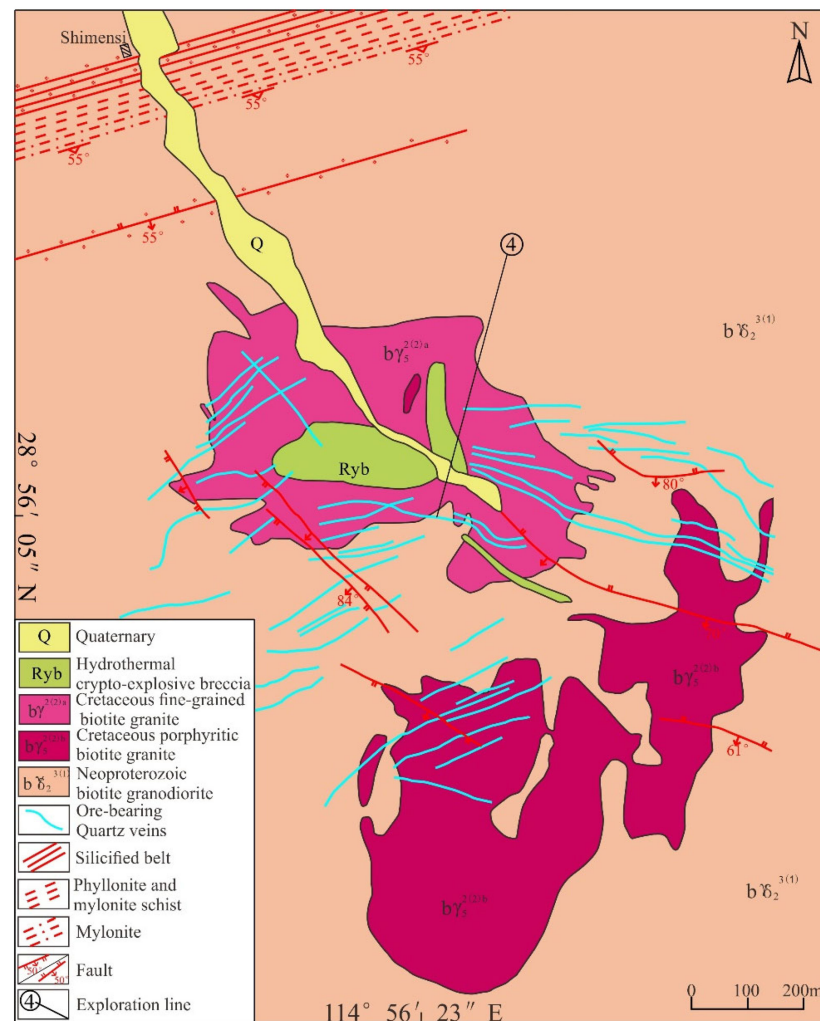


Figure 3. Geological map of the Shimensi deposit (modified after [12]).

Three types of mineralization can be identified at Shimensi, i.e., veinlet-disseminated, hydrothermal crypto-explosive breccia and quartz vein, which commonly coexist spatially and overlap one another (Figures 4 and 5). The veinlet-disseminated orebodies, accounting for over 90% of the W reserve, are distributed in the Neoproterozoic biotite granodiorite and Mesozoic granitic rocks (Figure 5a,b), especially in their exo-contact zone. The ore minerals are mainly scheelite with minor wolframite and chalcopyrite, which intergrow with some sulfides, including molybdenite, pyrrhotite, arsenopyrite, bornite, sphalerite, pyrite, enargite and tennantite. Major non-metallic minerals include quartz, biotite, muscovite, K-feldspar, dolomite and fluorite [22]. Alteration is closely related to wall rock lithology: K-feldspar is present in the contact zone close to the Mesozoic porphyritic biotite granite, whereas biotite is present close to Neoproterozoic biotite granodiorite. Greisenization and chlorite were developed in both the endo- and exo-contacts.

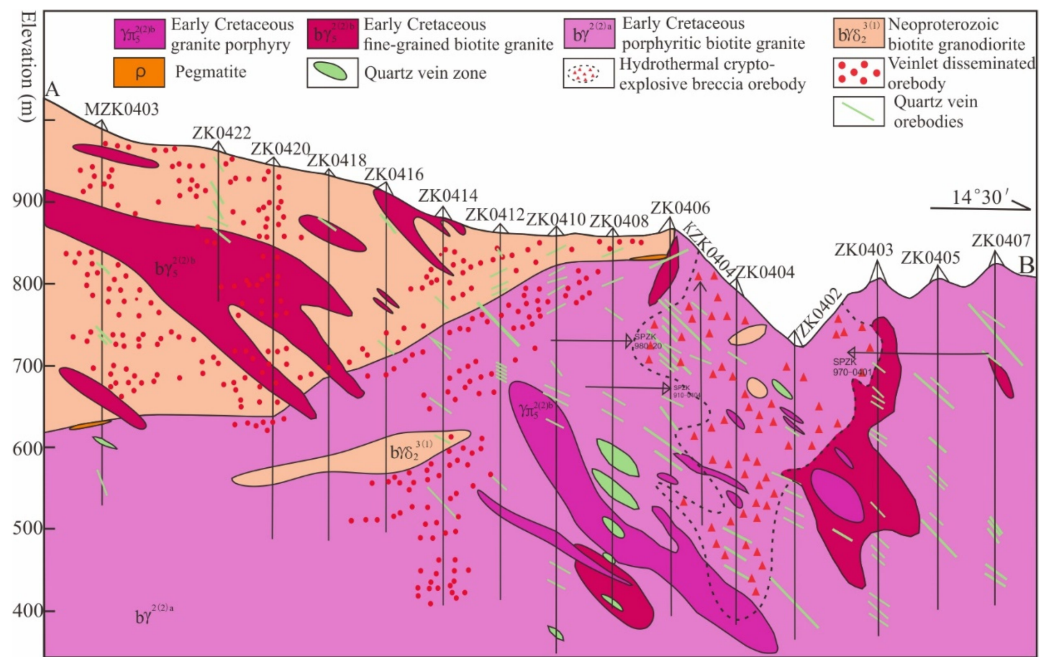


Figure 4. Geological map of the Shimensi No. 4 prospecting line, showing the three ore types: veinlet-disseminated, hydrothermal crypto-explosive breccia and quartz veins.

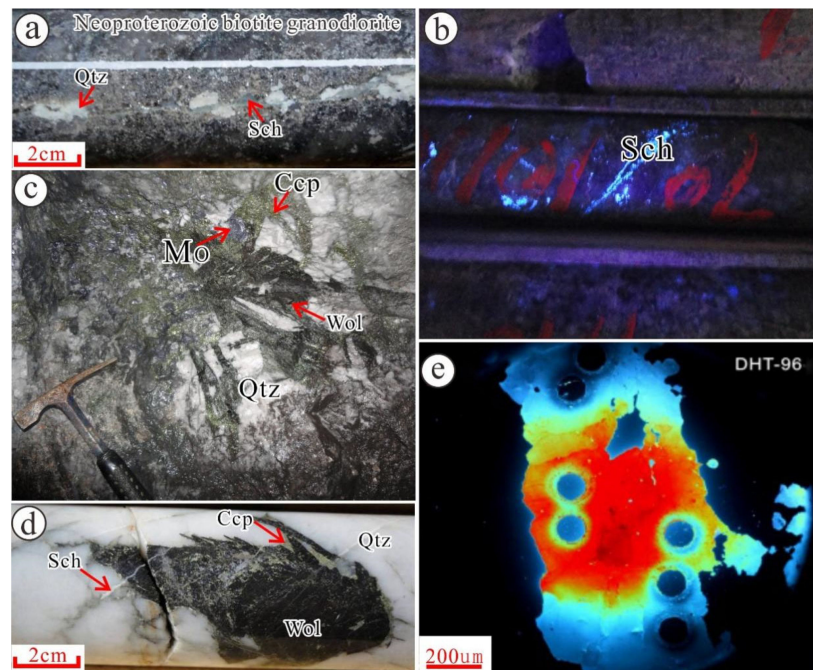


Figure 5. Photos of the representative rocks and ores obtained from the Shimensi deposit: (a,b) veinlet-disseminated scheelite in Neoproterozoic biotite granodiorite; (c) mineralization in hydrothermal crypto-explosive breccia; (d) scheelite and wolframite in quartz veins, wolframite cut by nearly parallel scheelite veins; (e) CL image of veinlet-disseminated scheelite. Qtz = quartz, Sch = scheelite, Cpy = chalcopyrite, Wol = wolframite, Mo = molybdenite.

Hydrothermal crypto-explosive breccia orebodies in central Shimensi lie mainly over the Mesozoic porphyritic biotite granite, and partially extend into the Neoproterozoic biotite granodiorite. This type accounts for approximately 5% of the total W reserve. The breccia clasts were derived mainly from the Neoproterozoic granodiorite and less from the Mesozoic

porphyritic biotite granite. The felsic matrix comprises mainly quartz, together with scheelite, molybdenite, chalcopyrite, bornite and minor wolframite (Figure 5c). The alteration mainly consists of K-feldspar and greisenization, with minor fluorite and tourmaline.

The quartz-vein orebodies are distributed throughout central Shimensi and cut the orebodies of other types. These veins are typically parallel to each other, mostly 100–200 m long and 20–40 cm wide. The orebodies have higher WO_3 and Cu grades than the other mineralization styles. Ore minerals mainly include wolframite and scheelite, with minor chalcopyrite (Figure 5d). Non-metallic minerals include quartz, muscovite and calcite. K-feldspar and greisen alterations are the main wall-rock alteration styles, and are accompanied by weak albite, chlorite and carbonate alterations.

4. Sampling and Analytical Methods

4.1. Sampling

A total of eight scheelite samples for trace element analysis were taken from the drill cores ZK11214 and ZK11612, including five veinlet-disseminated scheelite samples (DHT91, DHT96, DHT198, DHT202 and DHT204) and three quartz-vein-hosted scheelite samples (DHT231, DHT233 and DHT241). A total of 38 least-altered samples were selected for Pb isotope analysis, including scheelite ($n = 13$), wolframite ($n = 2$), molybdenite ($n = 4$), chalcopyrite ($n = 3$), biotite granodiorite ($n = 4$), porphyry biotite granite ($n = 4$), fine-grained biotite granite ($n = 4$) and granite porphyry ($n = 4$). Meanwhile, 9 scheelite samples were also analyzed for their O isotopes.

4.2. Analytical Methods

Electron microprobe (EPMA) analysis of the samples was conducted at the Wuhan Center of Geological Survey, China Geological Survey, using a JEOL JXA8100 electron probe microanalyzer (EPMA; JEOL, Japan). The EPMA was operated at 15 kV accelerating voltage with 10 nA beam current, 5 μm beam size and 10–30 s counting time. All data were corrected using the ZAF procedure. The detection limit is 0.01% for most elements, except for Mo and Ti (0.02%).

Scheelite cathodoluminescence (CL) imaging and in situ LA-ICP-MS analysis were conducted at the Key Laboratory of Orogenic Belts and Crustal Evolution, Ministry of Education, Peking University. A Gatan Chromal CL cold cathode generator and an FEI Quanta FEG 650 scanning electron microscope (SEM; FEI, Hillsboro, America) were used for the imaging. SEM was operated at ~12 keV under a vacuum of ~30 Pa. LA-ICP-MS in situ analysis of scheelite trace elements was performed on a 193 nm ArF excimer laser ablation system, connected to an Agilent 7500a ICP-MS (Agilent Technologies, Palo Alto, America) with a transfer tube. Helium was used as the carrier gas, which mixed with argon make-up gas via a T-connector before entering the ICP. The carrier and make-up gas flows were optimized by ablating the NIST SRM 610 standard, in order to obtain the maximum signal intensity while keeping the ThO/Th (0.1–0.3%) ratio low to reduce the oxide and doubly charged ion interference. Each LA-ICP-MS analysis comprised a ~20 s background acquisition (gas blank) followed by a 60 s sample data acquisition. Every tenth spot analysis was followed by one NIST SRM 610 standard analysis to correct the time-dependent drift of sensitivity and mass discrimination of the ICP-MS. Reference glasses (GSE, NIST612 and NIST614) were analyzed prior to and following the sample measurements.

The lead and oxygen isotope analyses were performed at the Beijing Research Institute of Uranium Geology. The scheelite O isotope compositions were measured using a MAT-253 mass spectrometer (Finnigan MAT, Bremen, German). The analytical precision for $\delta^{18}\text{O}$ was $\pm 0.5\%$. The Pb isotopes of sulfide separates were measured on a GV Isoprobe-T thermal ionization mass spectrometer (TIMS; GV, Manchester, British). The measurement precision for $^{204}\text{Pb}/^{206}\text{Pb}$ was less than 0.05%, with $^{208}\text{Pb}/^{206}\text{Pb}$ generally no more than 0.005% for 1 μg Pb. Detailed analytical procedures are described by Zhu et al. [36] and Yang et al. [37].

5. Results

5.1. Scheelite Geochemistry

5.1.1. Cathodoluminescence Image

The scheelite samples varied from red to yellow to blue (most common) under CL imaging. The scheelite grains with red CL had the highest total REE content (ΣREE = avg. 1315.24 ppm, data obtained from LA-ICP-MS), whilst those with blue CL images had the lowest ΣREE (avg. 76.41 ppm, data obtained from LA-ICP-MS). Scheelite samples with yellow CL images presented intermediate ΣREE content. Scheelites with red and yellow CL images presented positive and negative Eu anomalies, respectively, whilst those with blue CL images presented only indistinct Eu anomalies (Figure 5e).

5.1.2. Major and Trace Elements

EPMA analysis indicates that Scheelite has concentrations of WO_3 and CaO of 76.79–79.12 wt.% and 19.68–21.65 wt.%, respectively. The molybdenum oxide (MoO_3) content varied from <0.01 to 0.05 wt.%. In addition, all the scheelite samples contained small quantities of MnO and FeO.

A total of 71 laser spots were performed by LA-ICP-MS on the Shimensi scheelite samples (Supplementary Table S1). The ΣREE contents significantly fluctuated in different samples (9.88–2548.12 ppm, avg. 654.28 ppm; Table 1). For example, sample DHT-241 had ΣREE = 9.88–136.32 ppm (avg. 76.41 ppm), whereas sample DHT-202 has ΣREE = 394.6–2548.12 ppm (avg. 1362.96 ppm) (Table 1). In the chondrite-normalized REE patterns (Figure 6), most samples were characterized by LREE/HREE enrichment (La_N/Yb_N = 1.1–137.4), but four samples presented LREE/HREE depletions (La_N/Yb_N = 0.61–0.78). Meanwhile, the samples displayed Eu anomalies (δEu = 0.12–12.57, both negative ($n = 20$) and positive ($n = 51$)). It was noteworthy that the samples with higher ΣREE values presented negative Eu anomalies, and vice versa. Significant inter- and intra-grain REE variation occurred in our samples, and according to the REE features the samples could be divided into three types (SchI, SchII and SchIII): SchI has high ΣREE (394.60–2548.12 ppm, avg. 1315.24 ppm) and positive Eu anomalies; SchII (uncommon) has intermediate ΣREE content and weak positive/negative Eu anomalies; SchIII has the lowest ΣREE value (9.88–136.32 ppm, avg. 76.41 ppm) and negative Eu anomalies. For individual REE content, sample DHT241 had 0.34–8.34 (avg. 2.72) ppm Sm and 1.42–33.08 (avg. 13.13) ppm Nd, whereas sample DHT91 had 14.68–98.13 (avg. 67.75) ppm Sm and 1.42–33.08 (231.38) ppm Nd. However, the Sm/Nd range for an individual sample was narrow (0.14–0.37).

Table 1. Summary of statistics for trace element data set of the Shimensi scheelite (ppm).

Elements	DHT91 (n = 6)				DHT96 (n = 10)				DHT198 (n = 10)				DHT202 (n = 12)			
	Max	Min	Ave	Std	Max	Min	Ave	Std	Max	Min	Ave	Std	Max	Min	Ave	Std
Ti	2.79	0.36	0.94	0.92	0.35	0.10	0.19	0.08	0.73	0.13	0.37	0.22	31.65	0.10	3.87	10.42
Sr	120.80	62.02	84.89	24.81	460.06	196.03	353.98	75.93	369.23	182.41	273.60	62.64	198.37	29.31	133.87	65.32
Y	802.65	177.57	616.01	235.04	167.17	87.53	123.48	22.57	255.49	156.88	201.98	33.16	876.26	74.33	395.84	269.02
Nb	95.07	27.30	51.65	27.13	14.72	2.45	5.23	3.98	5.56	2.99	3.96	0.68	149.28	9.33	59.38	54.01
Mo	294.40	2.43	94.21	141.89	163.74	107.53	138.17	19.93	149.82	129.60	140.91	6.96	102.55	28.76	76.35	22.66
Ba	0.28	0.05	0.12	0.08	0.55	0.08	0.21	0.17	0.14	0.02	0.07	0.04	0.08	0.01	0.04	0.02
La	165.75	55.32	96.58	49.10	96.62	56.95	78.21	12.52	126.86	95.05	111.75	11.14	787.42	88.30	265.08	200.13
Ce	489.20	136.19	336.25	127.29	187.82	125.18	149.95	17.18	409.60	245.75	313.21	54.73	1234.60	181.02	501.39	275.12
Pr	61.89	16.23	48.61	17.16	20.45	12.47	16.62	2.55	65.89	28.36	43.55	12.64	98.26	14.17	54.32	23.33
Nd	301.33	63.70	231.38	97.38	91.32	40.03	63.12	15.13	329.86	105.19	193.22	81.75	393.34	35.49	213.62	123.98
Sm	98.13	14.68	67.75	34.76	25.71	7.63	15.14	5.11	81.94	23.85	46.52	20.89	132.27	6.15	59.08	49.17
Eu	23.39	8.44	16.72	4.94	13.70	7.27	9.40	2.09	21.33	11.19	14.45	3.73	26.73	5.32	12.71	7.16
Gd	127.75	13.82	82.59	47.19	29.27	6.77	15.43	6.39	79.96	22.48	44.80	20.79	161.59	4.75	64.80	64.89
Tb	26.63	3.14	17.54	9.61	5.41	1.42	3.02	1.17	12.94	4.72	8.11	2.98	30.34	0.95	12.44	12.43
Dy	198.23	27.95	132.33	68.89	33.51	9.81	19.63	7.11	75.28	30.22	49.78	16.11	199.11	6.12	78.79	79.38
Ho	41.14	6.94	27.59	13.54	6.86	2.14	4.09	1.41	14.90	6.56	10.09	3.03	43.61	1.33	16.18	16.49
Er	114.75	28.43	80.35	33.45	17.05	6.88	11.45	3.23	35.20	18.58	25.92	6.17	113.11	4.26	41.90	40.31
Tm	13.70	5.57	10.47	3.15	2.36	1.28	1.88	0.37	4.52	2.71	3.42	0.61	13.35	0.87	5.56	4.31
Yb	76.39	49.87	64.41	11.66	19.09	10.83	15.14	2.36	28.22	15.39	19.75	3.70	68.51	6.79	33.29	19.62
Lu	8.53	5.39	7.24	1.08	2.67	1.56	2.18	0.34	3.49	1.71	2.43	0.48	7.49	0.96	3.79	1.95
Ta	9.38	6.71	8.03	1.05	10.57	9.04	9.68	0.43	9.73	7.92	8.92	0.55	12.73	9.02	10.75	1.21
ΣREE	1567.81	438.70	1219.79	452.88	493.58	319.18	405.24	52.62	1268.63	627.08	886.99	224.59	2548.12	394.60	1362.96	566.61
La _N / Yb _N	2216.90	282.02	1479.86	803.80	543.16	142.31	302.33	113.42	1602.70	458.47	903.86	412.58	2894.70	107.02	1219.24	1121.82
δEu	1.79	0.48	0.92	0.55	3.03	1.24	2.01	0.54	1.81	0.64	1.06	0.33	4.22	0.12	1.64	1.37

Element	DHT204 (n = 10)				DHT231 (n = 7)				DHT233 (n = 4)				DHT241 (n = 12)			
	Max	Min	Ave	Std	Max	Min	Ave	Std	Max	Min	Ave	Std	Max	Min	Ave	Std
Ti	0.42	0.09	0.24	0.12	1.98	0.08	0.87	0.91	2.98	0.44	1.85	1.21	7.99	0.09	1.39	2.35
Sr	198.67	124.53	167.22	22.33	1581.63	88.21	749.71	723.32	200.79	139.52	161.63	26.89	185.41	94.51	141.09	35.13
Y	196.17	104.00	147.04	29.40	112.82	11.47	53.74	40.61	38.08	30.38	33.32	3.68	23.92	1.45	7.35	7.10
Nb	34.44	8.10	17.35	8.67	63.05	11.09	32.08	19.49	219.04	23.81	115.12	83.43	2.02	1.29	1.58	0.23
Mo	98.51	68.80	88.33	8.68	7.84	0.41	2.30	2.74	6.84	1.11	2.66	2.80	3.76	0.39	1.73	1.12
Ba	0.06	0.02	0.03	0.02	0.12	0.02	0.08	0.04	0.27	0.08	0.16	0.08	0.64	0.02	0.23	0.23
La	305.76	140.98	216.44	63.68	83.39	12.66	56.15	27.36	109.66	39.89	81.87	31.38	28.27	2.84	16.99	8.12
Ce	468.25	165.60	297.80	100.80	105.78	26.56	71.13	32.60	100.46	53.77	86.25	21.91	57.80	4.04	34.36	19.14
Pr	36.83	10.63	23.40	10.22	8.91	2.29	5.27	2.51	6.89	4.14	5.73	1.15	7.72	0.42	3.73	2.43
Nd	106.98	19.79	60.58	32.53	23.44	6.71	13.02	6.59	17.67	11.57	14.38	2.51	33.08	1.42	13.13	10.02
Sm	22.66	2.98	11.14	6.96	8.69	1.65	3.68	2.63	2.90	1.73	2.24	0.49	8.34	0.34	2.72	2.53
Eu	13.63	7.17	10.23	2.03	10.27	1.68	5.18	3.15	2.49	1.00	2.07	0.72	2.32	0.09	0.81	0.85
Gd	17.27	2.50	8.60	5.27	10.74	1.41	4.16	3.41	2.88	2.03	2.40	0.35	6.36	0.27	2.02	2.04
Tb	3.89	0.58	1.80	1.10	3.25	0.30	1.14	1.04	0.73	0.51	0.64	0.11	0.83	0.04	0.27	0.28
Dy	25.25	4.28	12.03	6.81	24.15	2.25	8.37	7.61	6.70	4.64	5.66	1.02	3.67	0.17	1.26	1.31
Ho	4.91	1.09	2.54	1.24	4.95	0.52	1.80	1.52	1.73	1.20	1.45	0.25	0.58	0.03	0.19	0.19
Er	14.34	3.98	8.10	3.16	15.17	2.06	6.10	4.48	6.79	4.53	5.49	1.11	1.36	0.07	0.45	0.45
Tm	2.45	1.01	1.66	0.43	2.78	0.54	1.34	0.77	1.54	1.04	1.24	0.23	0.19	0.01	0.06	0.06
Yb	19.70	10.32	14.26	3.40	19.10	6.01	12.35	5.13	16.00	10.99	12.60	2.35	1.29	0.10	0.37	0.35
Lu	2.96	1.28	1.90	0.59	2.55	0.93	1.74	0.64	2.65	1.66	1.93	0.48	0.18	0.02	0.05	0.05
Ta	10.83	8.67	9.66	0.64	9.27	8.56	8.95	0.26	26.19	9.82	16.55	7.10	9.06	7.88	8.61	0.34
ΣREE	969.93	375.27	670.46	204.24	310.08	75.94	191.44	89.45	261.44	150.58	223.94	49.91	136.32	9.88	76.41	45.03
La _N / Yb _N	391.69	55.54	193.61	119.78	191.28	30.20	77.28	59.43	57.22	39.84	45.77	7.97	144.20	6.08	46.25	44.99
δEu	12.57	1.93	4.92	3.91	1.41	0.76	1.02	0.25	1.29	0.72	0.92	0.25	7.39	0.72	3.50	1.76

Abbreviations: Min = minimum; Max = maximum; Ave = average; Std = standard deviation.

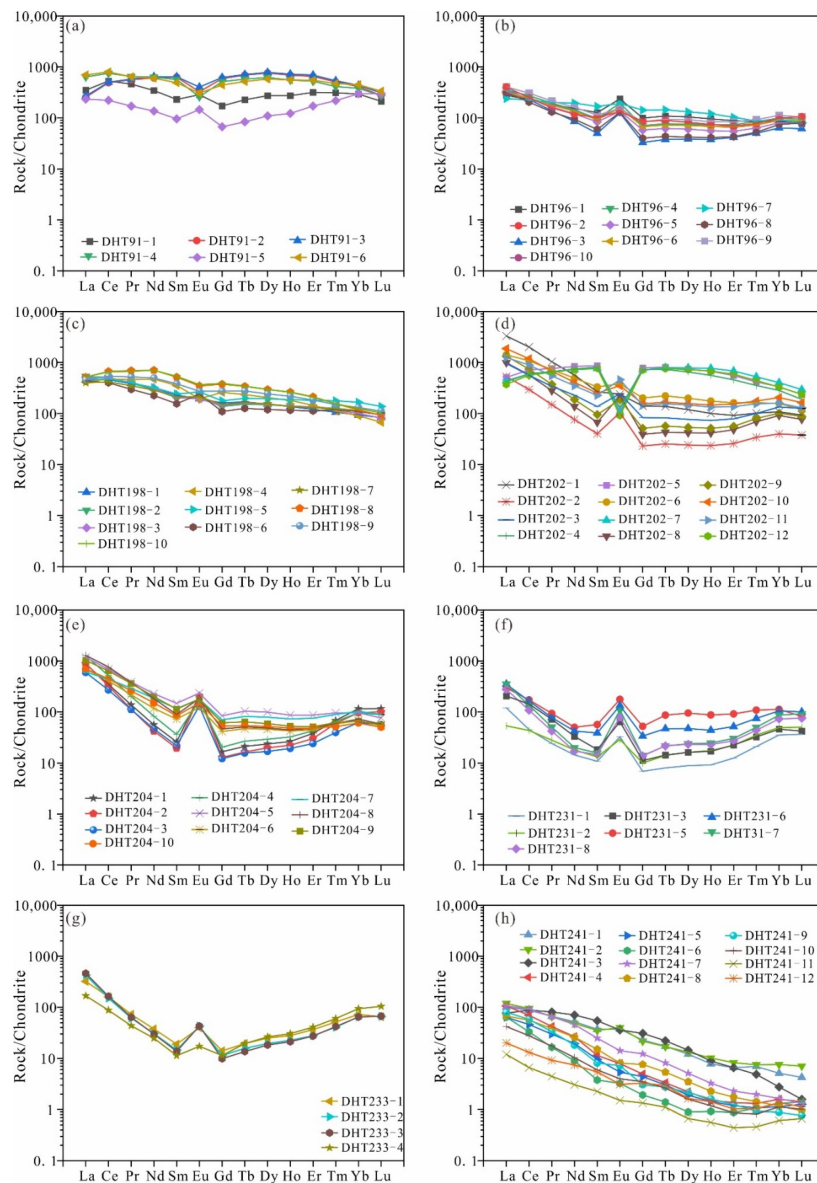


Figure 6. Chondrite-normalized REE patterns of scheelite from the Shimensi deposit: (a) DHT91; (b) DHT96; (c) DHT198; (d) DHT202; (e) DHT204; (f) DHT231; (g) DHT233; (h) DHT241. Data of (d–g) are adapted from [19]. Normalizing values are from Sun and McDonough [38].

5.2. Lead Isotopes

Scheelite: The Pb isotope variation range of most scheelite samples (n = 9) was narrow, with $^{206}\text{Pb}/^{204}\text{Pb} = 18.286$ to 19.661 (avg. 18.525), $^{207}\text{Pb}/^{204}\text{Pb} = 15.644$ to 15.739 (avg. 15.666) and $^{208}\text{Pb}/^{204}\text{Pb} = 38.265$ to 38.797 (avg. 38.561), respectively (Table 2).

Wolframite: The samples had $^{206}\text{Pb}/^{204}\text{Pb} = 18.219$ to 18.245 (avg. 18.232), $^{207}\text{Pb}/^{204}\text{Pb} = 15.623$ to 15.628 (avg. 15.626) and $^{208}\text{Pb}/^{204}\text{Pb} = 38.429$ to 38.451 (avg. 38.440), respectively (Table 2).

Molybdenite: The samples had $^{206}\text{Pb}/^{204}\text{Pb} = 18.184$ to 18.204 (avg. 18.193), $^{207}\text{Pb}/^{204}\text{Pb} = 15.605$ to 15.654 (avg. 15.624) and $^{208}\text{Pb}/^{204}\text{Pb} = 38.439$ to 38.489 (avg. 38.460), respectively (Table 2).

Chalcopyrite: The samples had $^{206}\text{Pb}/^{204}\text{Pb} = 18.199$ to 19.093 (avg. 18.508), $^{207}\text{Pb}/^{204}\text{Pb} = 15.624$ to 15.670 (avg. 15.650) and $^{208}\text{Pb}/^{204}\text{Pb} = 38.504$ to 38.942 (avg. 38.701), respectively (Table 2).

Feldspar (obtained from Neoproterozoic biotite granodiorite): The samples had $^{206}\text{Pb}/^{204}\text{Pb} = 18.001$ to 18.211 (avg. 18.107), $^{207}\text{Pb}/^{204}\text{Pb} = 15.617$ to 15.649 (avg. 15.626) and $^{208}\text{Pb}/^{204}\text{Pb} = 38.000$ to 38.287 (avg. 38.112), respectively (Table 2).

Feldspar (obtained from Mesozoic porphyritic biotite granite): The samples had $^{206}\text{Pb}/^{204}\text{Pb} = 18.371$ to 18.491 (avg. 18.438), $^{207}\text{Pb}/^{204}\text{Pb} = 15.625$ to 15.645 (avg. 15.636) and $^{208}\text{Pb}/^{204}\text{Pb} = 38.533$ to 38.637 (avg. 38.606), respectively (Table 2).

Feldspar (obtained from Mesozoic fine-grained biotite granite): The samples had $^{206}\text{Pb}/^{204}\text{Pb} = 18.280$ to 18.410 (avg. 18.340), $^{207}\text{Pb}/^{204}\text{Pb} = 15.614$ to 15.647 (avg. 15.627) and $^{208}\text{Pb}/^{204}\text{Pb} = 38.521$ to 38.626 (avg. 38.569), respectively (Table 2).

Feldspar (obtained from Mesozoic granite porphyry): The samples had $^{206}\text{Pb}/^{204}\text{Pb} = 18.410$ to 18.877 (avg. 18.663), $^{207}\text{Pb}/^{204}\text{Pb} = 15.645$ to 15.681 (avg. 15.662) and $^{208}\text{Pb}/^{204}\text{Pb} = 38.527$ to 38.685 (avg. 38.663), respectively (Table 2).

Table 2. Lead isotope values of the ore minerals (scheelite, wolframite, molybdenite and chalcopyrite) and feldspar obtained from the Shimensi tungsten deposit.

Sample No.	Mineral	Ore or Rock Type	$^{206}\text{Pb}/^{204}\text{Pb}$	$^{207}\text{Pb}/^{204}\text{Pb}$	$^{208}\text{Pb}/^{204}\text{Pb}$	Sample No.	Mineral	Ore or Rock Type	$^{206}\text{Pb}/^{204}\text{Pb}$	$^{207}\text{Pb}/^{204}\text{Pb}$	$^{208}\text{Pb}/^{204}\text{Pb}$
SMT1	Scheelite	Veinlet disseminated	18.521	15.670	38.797	SM11	Feldspar	Fine-grained biotite granite	18.350	15.624	38.589
SMT2	Scheelite	Veinlet disseminated	18.322	15.646	38.567	SM12	Feldspar	Fine-grained biotite granite	18.280	15.614	38.521
SMT3	Scheelite	Veinlet disseminated	18.339	15.671	38.533	SM31	Feldspar	Fine-grained biotite granite	18.410	15.647	38.626
SMT4	Scheelite	Veinlet disseminated	18.286	15.657	38.514	SM52	Feldspar	Fine-grained biotite granite	18.321	15.622	38.540
SMT5	Scheelite	Veinlet disseminated	18.462	15.666	38.677	SM29	Feldspar	Granite porphyry	18.877	15.645	38.527
SMT6	Scheelite	Veinlet disseminated	18.348	15.644	38.455	SM30	Feldspar	Granite porphyry	18.669	15.681	38.685
SMT7	Scheelite	Veinlet disseminated	18.305	15.652	38.557	SM32	Feldspar	Granite porphyry	18.410	15.656	38.609
SMT8	Scheelite	Veinlet disseminated	18.478	15.652	38.687	SM51	Feldspar	Granite porphyry	18.697	15.665	38.631
SMT9	Scheelite	Veinlet disseminated	19.661	15.739	38.265	Wo-1	Wolframite	Thick quartz vein	18.219	15.623	38.429
SM18	Feldspar	Biotite granodiorite	18.202	15.617	38.048	Wo-2	Wolframite	Thick quartz vein	18.245	15.628	38.451
SM19	Feldspar	Biotite granodiorite	18.211	15.649	38.287	Mo-1	Molybdenite	Thick quartz vein	18.204	15.654	38.453
SM49	Feldspar	Biotite granodiorite	18.015	15.621	38.112	Mo-2	Molybdenite	Veinlet disseminated	18.184	15.605	38.439
SM54	Feldspar	Biotite granodiorite	18.001	15.617	38.000	Mo-3	Molybdenite	Veinlet disseminated	18.19	15.613	38.459
SM05	Feldspar	Porphyritic biotite granite	18.371	15.625	38.553	Mo-4	Molybdenite	Hydrothermal crypto-explosive breccia	18.194	15.622	38.489
SM50	Feldspar	Porphyritic biotite granite	18.454	15.627	38.604	Ch-1	Chalcopyrite	Thick quartz vein	18.233	15.67	38.657
SM56	Feldspar	Porphyritic biotite granite	18.491	15.645	38.631	Ch-2	Chalcopyrite	Thick quartz vein	18.199	15.624	38.504
SM57	Feldspar	Porphyritic biotite granite	18.437	15.645	38.637	Ch-3	Chalcopyrite	Hydrothermal crypto-explosive breccia	19.093	15.657	38.942

5.3. Oxygen Isotope Compositions

The $\delta^{18}\text{O}$ variation range of the scheelite samples was narrow, with the scheelite $\delta^{18}\text{O} = 4.30$ – 6.50 ‰ (avg. 5.71 ‰, $n = 9$) (Table 3). The highest homogenization temperature of 375 °C in fluid inclusions of quartz that intergrows with scheelite [2] was used to calculate the $\delta^{18}\text{O}$ water values of fluid based on the scheelite–H₂O fractionation equilibrium [39]. The hydrothermal fluid had $\delta^{18}\text{O} = 7.0$ – 9.6 ‰ (avg. 8.3 ‰, $n = 9$) (Table 3).

6. Discussion

6.1. Substitution of REE for Ca in Scheelite

The substitution of REE^{3+} for Ca^{2+} in scheelite has been widely studied [19,40–47], and the possible mechanism can be expressed as follows:

- ① $2Ca^{2+} = REE^{3+} + Na^{+}$;
- ② $Ca^{2+} + W^{6+} = REE^{3+} + Nb^{5+}$;
- ③ $3Ca^{2+} = 2REE^{3+} + \square Ca$ ($\square Ca = Ca$ -site vacancy).

Mode ①: scheelite has high Na content. Meanwhile, the upward parabolic REE patterns in scheelite imply that MREEs occupy the Ca sites, as the ionic sizes of $MREE^{3+}$ (1.06Å) and Ca^{2+} (1.12Å) are similar [42]. For Shimensi, the low-salinity ore-forming fluids (0.88–9.47 wt% $NaCl_{eq}$; [2]) indicate low Na concentration. The low Na concentration and poor Na vs. REE correlation in all our samples indicate that Mode ① is unimportant for the REE incorporation.

Mode ②: the Nb concentration is high. Both HREEs and MREEs are relatively depleted (while LREEs are enriched) as a result of their substitution for Nb^{5+} [42,43]. Nb content for the scheelite samples (1.29–219.04 ppm) is much lower than the ΣREE content, and the lack of positive Nb^{5+} vs. ΣREE correlation in most samples suggests that Mode ② is unimportant (Figure 7a).

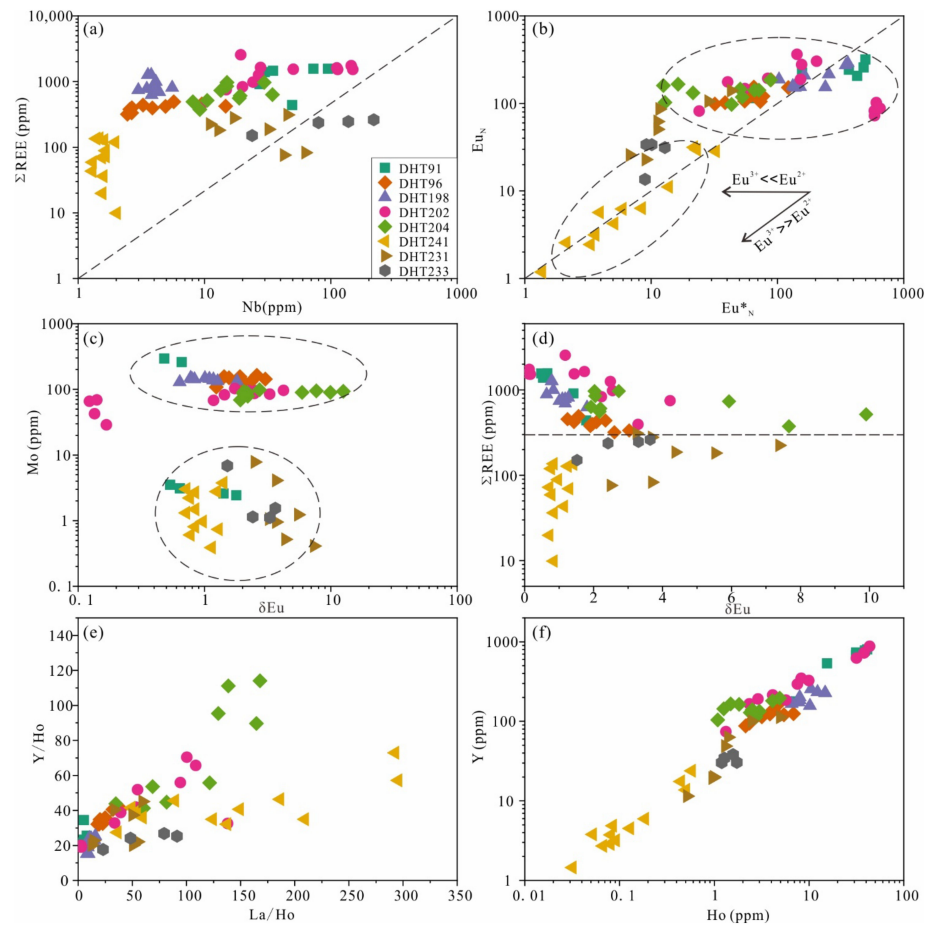


Figure 7. Plots of (a) Nb vs. ΣREE , showing no positive correlation for most of the scheelite samples; (b) chondrite-normalized Eu_N vs. calculated Eu^*_N values for scheelite ($Eu^*_N = (Sm_N \times Gd_N)^{1/2}$), showing that the majority of the spots are distributed along a horizontal line, while DHT141 shows positive Eu_N vs. Eu^*_N correlation; (c) δEu vs. Mo, showing that scheelite Mo content significantly decreases from the early to the late stage; (d) δEu vs. ΣREE , showing that the samples can be divided into two groups by ΣREE ; (e) La/Ho vs. Y/Ho, showing similar trends for most of the samples (except DHT-141); (f) Ho vs. Y, showing that most of the samples have positive Ho vs. Y correlation.

Table 3. Oxygen isotope data of scheelite obtained from the Shimensi tungsten deposit. (Data are adapted from [48]).

Sample No.	Mineral	$\delta^{18}\text{O}_{\text{scheelite}}$ (‰)	$\delta^{18}\text{O}_{\text{water}}$ (‰)
SMT1	Scheelite	6.1	7.7
SMT2	Scheelite	5.4	7.4
SMT3	Scheelite	4.8	7.2
SMT4	Scheelite	5.9	8.4
SMT5	Scheelite	4.3	7.0
SMT6	Scheelite	6.4	9.2
SMT7	Scheelite	6.4	9.4
SMT8	Scheelite	6.5	9.6
SMT9	Scheelite	5.6	8.8

Mode ③: the samples have low Na and Nb but high ΣREE contents, and no MREE-enriched patterns. Thus, Mode ③, in which REE ions are substituted into a vacant Ca site in pairs, could represent the best REE replacement mechanism.

6.2. Sources and Evolution of the Ore-Forming Fluid

The calculated $\delta^{18}\text{O}$ for ore-forming fluid is 7.0–9.6‰ and falls in the magmatic water range [49], which suggests a magmatic–hydrothermal fluid origin. However, the different trace and REE elements between veinlet-disseminated and quartz-vein-hosted scheelite (Figures 6 and 7) may indicate that the ore-forming fluid is not homogenous, which is consistent with the presence of a magmatic hydrothermal fluid as early ore-forming fluid and of a mixing of meteoric water as late ore-forming fluid, as shown by the study of quartz fluid inclusions and H-O isotopes [2].

Europium can substitute for Ca in scheelite both as Eu^{3+} and as Eu^{2+} . If it enters as Eu^{3+} , it behaves similarly to the other REE^{3+} elements and would not change the trend of Eu anomaly in the hydrothermal fluids; if it enters as Eu^{2+} , ore-fluid-positive Eu anomalies occur when $\text{Eu}^{2+} \gg \text{Eu}^{3+}$ [19,42]. In Figure 7b, most of the data are presented along a horizontal line, indicating the domination of Eu^{2+} in the ore-forming fluid. This is consistent with the mostly positive Eu anomalies of these scheelites (Figure 6). However, data projections of sample DHT241 show positive Eu_N vs. Eu^*_N correlation, suggesting that Eu is dominated by Eu^{3+} . Such a variation characteristically indicates the evolution of ore-forming fluids from reducing to oxidizing from the early to late stage. The significant decrease in scheelite Mo content from the early to late stage (Figure 7c) is in contrast with the influence of $f\text{O}_2$ variation [50–52]. Considering that the early-stage scheelite intergrows with molybdenite, an early-stage crystallization of molybdenite and Mo-rich scheelite could be imagined to significantly decrease the ore-fluid Mo content, and thus the Mo content of the late-stage scheelite, even in relatively oxidizing conditions.

As REE and Y have similar partition coefficients in fluid and scheelite, the Y/Ho and La/Ho ratios in the minerals crystallized at the same stage should be similar, but show negative correlation in the minerals crystallized at different stages [53]. The different slopes between Y/Ho and La/Ho (Figure 7e) and very wide range of scheelite Y/Ho ratios (Y/Ho = 15.24–114.02; Figure 7f) may also reflect that the scheelite samples were formed at different stages. The difference of complexing F^- and HCO_3^- would cause the differentiation between Y and Ho [20,54], although the two elements have the same valence state and similar ionic radius: Y/Ho is >28 when F^- is present in the fluid and <28 when HCO_3^- prevails. Therefore, the Y/Ho difference in the analyzed samples indicates that the early-stage and late-stage ore-forming fluid may have been relatively rich in F^- and HCO_3^- , respectively. The F^- in the early stage may have been gradually lost because of the fluorite crystallization, and greisenization. Meanwhile, meteoric water infiltration may have also led to the ore-fluid HCO_3^- increase.

6.3. Provenance of Metals

The Pb isotopic compositions of the major metallic minerals obtained from Shimensi (scheelite, wolframite, chalcopyrite and molybdenite) fall into three groups (Figure 8): (1) wolframite–chalcopyrite–molybdenite; (2) scheelite–chalcopyrite–molybdenite; and (3) scheelite–chalcopyrite; this can reflect both multiphase mineralization and multiple material sources.

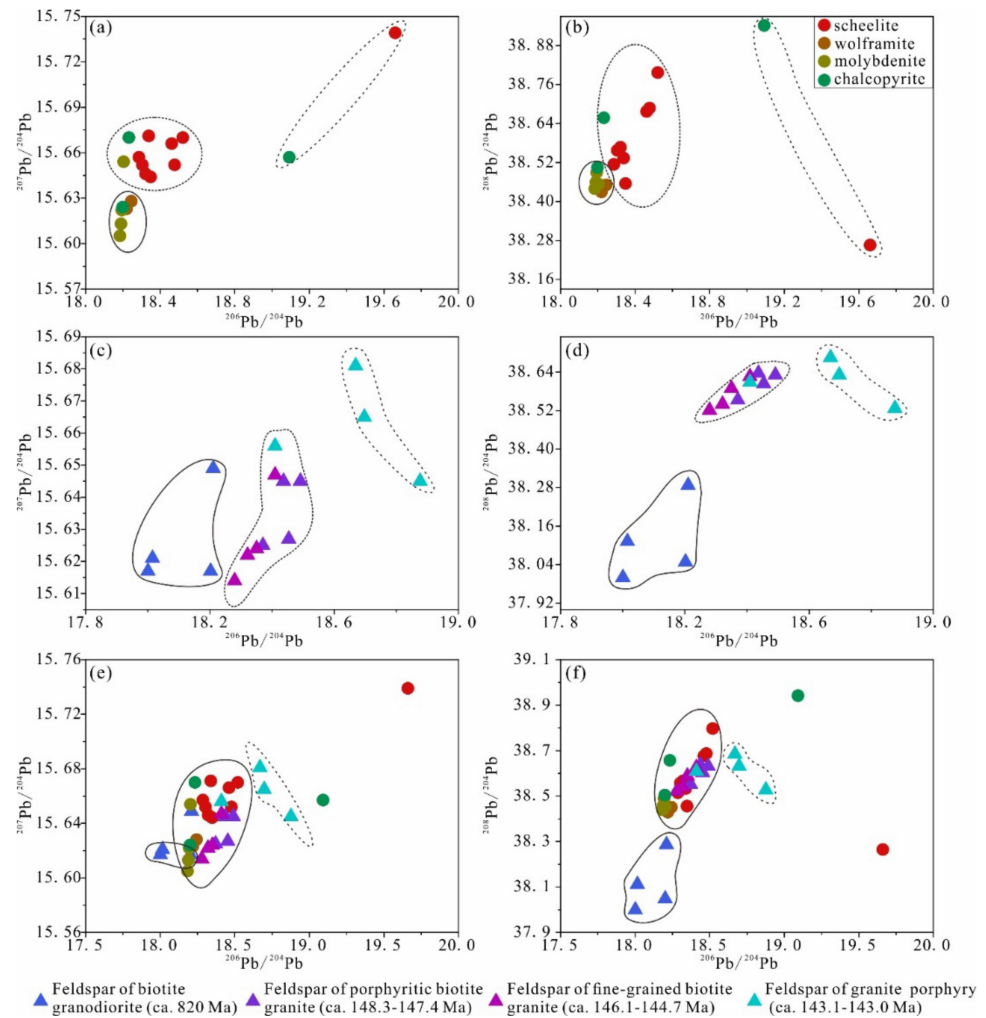


Figure 8. Plots of Pb isotope compositions of the (a,b) ore minerals (scheelite, wolframite, molybdenite and chalcopyrite) obtained from the Shimensi deposit; (c,d) feldspar obtained from the Neoproterozoic biotite granodiorite and Mesozoic granites at Shimensi; (e,f) ore minerals, the Neoproterozoic biotite granodiorite and Mesozoic granites at Shimensi. (Modified after [48]).

Due to the lack or minor presence of radiogenic Pb in the feldspar, the Pb isotope composition in the feldspar samples can approximate that present in the granite [55–57]. The Shimensi feldspar samples can also be divided into three Pb isotope compositional groups (Figure 8): (1) the compositions of the lead isotope in the Neoproterozoic biotite granodiorite, which has a lower radiogenic Pb content similar to the low-grade metamorphosed Shuangqiaoshan Group clastic rocks [58]. This is consistent with Sr-Nd isotopes of Neoproterozoic biotite granodiorite [33], indicating that Neoproterozoic biotite granodiorite is derived from the partial melting of the Shuangqiaoshan Group basement rocks. (2) The Mesozoic porphyritic/fine-grained biotite granites have similar Pb isotope compositions to most of the scheelite samples, which indicates that the main ore stage is closely

related to the granites. (3) The granite porphyry has a higher radiogenic Pb content than the porphyritic/fine-grained biotite granites.

As depicted in Figure 8, the Pb isotope compositions of the Shimensi metallic minerals are similar to those of the Early Cretaceous porphyritic/fine-grained biotite granites, suggesting that the latter two may have been the ore-forming material source. However, the lead isotopic compositions of the ore mineral, with higher radioactive lead values, are consistent with the compositions of the granite porphyry, which implies that granite porphyry may also play a role in the deposition of W mineralization.

As a result, we proposed that the veinlet-disseminated, hydrothermal crypto-explosive breccia and quartz-vein type mineralizations of the Shimensi deposit were formed in a uniform ore-forming system, which is related to the Mesozoic granites, especially Early Cretaceous porphyritic/fine-grained biotite granites. The high Ca Neoproterozoic biotite granodiorite is a high-quality surrounding rock, providing Ca to the scheelite. The contact zones between Mesozoic granites and Neoproterozoic biotite granodiorite are an optimal prospecting target for veinlet-disseminated and hydrothermal crypto-explosive breccia mineralization, whereas the fracture structures are good for quartz vein-type mineralization.

7. Conclusions

- (1) The acquired data reveal that $3\text{Ca}^{2+} = 2\text{REE}^{3+} + \square\text{Ca}$ ($\square\text{Ca}$ = Ca-site vacancy) was the principal substitution mechanism responsible for the REE fixation occurring in the Shimensi scheelite.
- (2) The Shimensi ore-forming fluid was mainly sourced from magmatic water, which possibly mixed with meteoric water in the late ore stage. The early-stage and late-stage ore-forming fluids may have been relatively rich in F^- and HCO_3^- , respectively, and evolved from reducing to oxidizing.
- (3) The Pb isotope compositions of the metallic minerals were similar to those of the porphyritic/fine-grained biotite granites. The main-stage ore-forming materials were consequently derived from these Mesozoic biotite granites.

Supplementary Materials: The following supporting information can be downloaded at: <https://www.mdpi.com/article/10.3390/min12111461/s1>, Table S1: Trace element data (ppm) of scheelite from the Shimensi tungsten deposit.

Author Contributions: Writing-original draft, P.W.; Writing-review & editing, P.W., T.L. and H.J.; Visualization, P.W. and H.J.; Investigation, X.X.; Formal analysis, B.Z. All authors have read and agreed to the published version of the manuscript.

Funding: The Mineral Geology of China Geological Survey (DD20190379, DD20160346), the Natural Science Basic Research Program of Shaanxi Science and Technology Department (2021JQ-985), the National Natural Science Foundation of China (41962012) and the Education Department of Jiangxi Province (GJJ190586).

Data Availability Statement: All data used in this study are freely available.

Acknowledgments: We thank Ma Zhendong (China University of Geosciences, Wuhan) and Liu Hanbin (Beijing Research Institute of Uranium Geology) for their valuable assistance during the fieldwork. We are grateful to editors and anonymous reviewers for their thoughtful reviews, that helped to significantly improve the manuscript.

Conflicts of Interest: The authors declare no conflict of interest.

References

1. Feng, C.Y.; Zhang, D.Q.; Xiang, X.K.; Li, D.X.; Qu, H.Y.; Liu, J.N.; Xiao, Y. Re-Os isotopic dating of molybdenite from the Dahutang tungsten deposit in northwestern Jiangxi Province and its geological implication. *Acta Petrol. Sin.* **2012**, *28*, 3858–3868. (In Chinese)
2. Wang, P. Geology, Fluid inclusion, Stable isotope and molybdenite Re-Os Constraints on the Genesis of the Shimensi Tungsten Metallogenic deposit, Northern Jiangxi Province. Master's Thesis, Sinosteel Tianjin Geological Academy, Tianjin, China, 2013; pp. 1–85. (In Chinese)

3. Jiang, S.Y.; Peng, N.J.; Huang, L.C.; Xu, Y.M.; Zhan, G.L.; Dan, X.H. Geological characteristic and ore genesis of the giant tungsten deposit from the Dahutang ore concentrated district in northern Jiangxi province. *Acta Petrol. Sin.* **2015**, *31*, 639–655. (In Chinese)
4. Sun, K.K.; Chen, B.; Deng, J. Ore genesis of the Zhuxi supergiant W-Cu skarn polymetallic deposit, South China: Evidence from scheelite geochemistry. *Ore Geol. Rev.* **2019**, *107*, 14–29. [[CrossRef](#)]
5. Feng, C.Y.; Wang, S.; Zeng, Z.L.; Zhang, D.Q.; Li, D.X.; She, H.Q. Fluid inclusion and chronology studies of Baxiannao mineralized fractured zone-type tungsten polymetallic deposit, southern Jiangxi province, China. *Acta Petrol. Sin.* **2012**, *28*, 52–64. (In Chinese)
6. Huang, L.C.; Jiang, S.Y. Zircon U-Pb geochronology, geochemistry and petrogenesis of the porphyric-like muscovite granite in the Dahutang tungsten deposit, Jiangxi Province. *Acta Petrol. Sin.* **2012**, *28*, 3887–3900. (In Chinese)
7. Huang, L.C.; Jiang, S.Y. Geochronology, geochemistry and petrogenesis of the tungsten-bearing porphyritic granite in the Dahutang tungsten deposit, Jiangxi Province. *Acta Petrol. Sin.* **2013**, *29*, 4323–4335. (In Chinese)
8. Huang, L.C.; Jiang, S.Y. Highly fractionated S-type granites from the giant Dahutang tungsten deposit in Jiangnan Orogen, Southeast China: Geochronology, petrogenesis and their relationship with W-mineralization. *Lithos* **2014**, *202*, 207–226. [[CrossRef](#)]
9. Mao, Z.H.; Cheng, Y.B.; Liu, J.J.; Yuan, S.D.; Wu, S.H.; Xiang, X.K.; Luo, X.H. Geology and molybdenite Re-Os age of the Dahutang granite-related veinlets-disseminated tungsten ore field in the Jiangxi Province, China. *Ore Geol. Rev.* **2013**, *53*, 422–433. [[CrossRef](#)]
10. Mao, Z.H.; Liu, J.J.; Mao, J.W.; Deng, J.; Zhang, F.; Meng, X.Y.; Xiong, B.K.; Xiang, X.K.; Luo, X.D. Geochronology and geochemistry of granitoids related to the giant Dahutang tungsten deposit, middle Yangtze River region, China: Implications for petrogenesis, geodynamic setting, and mineralization. *Gondwana Res.* **2014**, *7*, 1–21. [[CrossRef](#)]
11. Xiang, X.K.; Chen, M.S.; Zhan, G.N.; Qian, Z.Y.; Li, H.; Xu, J.H. Metallogenic geological conditions of Shimeisi tungsten-polymetallic deposit in north Jiangxi Province. *Contrib. Geol. Miner. Resour. Res.* **2012**, *27*, 143–155. (In Chinese)
12. Xiang, X.K.; Liu, X.M.; Zhan, G.N. Discovery of Shimensi super-large tungsten deposit and its prospecting significance in Dahutang area, Jiangxi Province. *Resour. Survey Environ.* **2012**, *33*, 141–151. (In Chinese)
13. Xiang, X.K.; Wang, P.; Sun, D.M.; Zhong, B. Isotopic Geochemical characteristics of the Shimensi tungsten-polymetallic deposit in northern Jiangxi Province. *Acta Geosci. Sin.* **2013**, *34*, 263–271. (In Chinese)
14. Xiang, X.K.; Wang, P.; Zhan, G.N.; Sun, D.M.; Zhong, B.; Qian, Z.Y.; Tan, R. Geological characteristics of Shimensi tungsten polymetallic deposit in Northern Jiangxi province. *Miner. Depos.* **2013**, *32*, 1171–1187. (In Chinese)
15. Gong, X.D.; Yan, G.S.; Ye, T.Z.; Zhu, X.Y.; Li, Y.S.; Zhang, Z.H.; Jia, W.B.; Yao, X.F. A study of ore-forming fluids in the Shimensi tungsten deposit, Dahutang tungsten polymetallic ore field, Jiangxi Province, China. *Acta Geol. Sin.* **2016**, *89*, 822–835.
16. Ye, Z.H.; Wang, P.; Xiang, X.K.; Yan, Q.; Li, Y.K.; Guo, J.H. Early Cretaceous tungsten mineralization in Southeastern China: The Wuning example. *Int. Geol. Rev.* **2016**, *59*, 946–964. [[CrossRef](#)]
17. Wei, W.F.; Lai, C.K.; Yan, B.; Zhu, X.; Song, S.; Liu, L. Petrogenesis and metallogenic implications of Neoproterozoic granodiorite in the super-large Shimensi tungsten-copper deposit in northern Jiangxi, South China. *Minerals* **2018**, *8*, 429. [[CrossRef](#)]
18. Wei, W.F.; Shen, N.P.; Yan, B.; Lai, C.K.; Yang, J.H.; Gao, W.; Liang, F. Petrogenesis of ore-forming granites with implications for W-mineralization in the super-large Shimensi tungsten-dominated polymetallic deposit in northern Jiangxi Province, South China. *Ore Geol. Rev.* **2018**, *95*, 1123–1139. [[CrossRef](#)]
19. Sun, K.K.; Chen, B. Trace elements and Sr-Nd isotopes of scheelite: Implications for the W-Cu-Mo polymetallic mineralization of the Shimensi deposit, South China. *Am. Mineral.* **2017**, *102*, 1114–1128.
20. Chen, C.F.; Gao, J.F.; Zhang, Q.Q.; Min, K. Evolution of ore-forming fluids in Shimensi tungsten polymetallic deposit of northern Jiangxi: Constraints from in situ trace element analysis of scheelite. *Miner. Depos.* **2021**, *40*, 293–310. (In Chinese)
21. Chen, X.Y.; Chen, G.H.; Shu, L.M.; Yao, J.L.; Shu, L.S. A Study of the Collision Timing of Yangtze and Cathaysia Blocks in the Eastern Jiangnan Orogenic Belt, South China. *Xinjiang Geol.* **2015**, *33*, 520–528. (In Chinese)
22. Zhang, Z.H.; Zhang, D.; Xiang, X.K.; Zhu, X.Y.; He, X.L. Geology and mineralization of the supergiant Shimensi granitic-type W-Cu-Mo deposit (1.168 Mt) in northern Jiangxi, South China: A Review. *China Geol.* **2022**, *5*, 510–527.
23. Wang, J.; Liu, B.J.; Pan, G.T. Neoproterozoic Rifting history of South China significance to Rodinia breakup. *J. Miner. Petrol.* **2001**, *21*, 135–145. (In Chinese)
24. Xue, H.M.; Ma, F.; Song, Y.Q.; Xie, Y.P. Geochronology and geochemistry of the Neoproterozoic granitoid association from eastern segment of the Jiangnan orogen, China: Constraints on the timing and process of amalgamation between the Yangtze and Cathaysia blocks. *Acta Petrol. Sin.* **2010**, *26*, 3215–3244. (In Chinese)
25. Zhou, J.C.; Wang, X.L.; Qiu, J.S. *The Neoproterozoic Tectonic-Magmatic Evolution of the Jiangnan Orogen Belt*; Science Press: Beijing, China, 2014. (In Chinese)
26. Deng, Q.; Wang, J.; Wang, Z.J.; Cui, X.Z.; Shi, M.F.; Du, Q.D.; Ma, L.; Liao, S.Y.; Ren, G.M. Middle Neoproterozoic magmatic activities and their constraints on tectonic evolution of the Jiangnan orogen. *Geotecton. Metallog.* **2016**, *40*, 753–771. (In Chinese)
27. Gao, L.Z.; Yang, M.G.; Ding, X.Z.; Liu, Y.X.; Liu, X.; Ling, L.H.; Zhang, C.H. SHRIMP U-Pb zircon dating of tuff in the Shuangqiaoshan and Heshangzhen groups in South China—Constraints on the evolution of the Jiangnan Neoproterozoic orogenic belt. *Geol. Bull. China* **2008**, *27*, 1744–1751. (In Chinese)
28. Liu, Y.G. *Rocks and Formations in Jiangxi Province*; China University of Geosciences Press: Wuhan, China, 1997; 381p. (In Chinese)
29. Wang, J.; Li, Z.X. History of Neoproterozoic rift basins in South China: Implications for Rodinia break-up. *Precambrian Res.* **2013**, *222*, 141–158. [[CrossRef](#)]
30. Huang, X.B.; Yu, Z.Z.; Zhou, G.Q. Sedimentary features of the Mesoproterozoic Shuangqiaoshan Group in northwestern Jiangxi. *Geol. Bull. China* **2003**, *22*, 43–49. (In Chinese)

31. Zuo, Q.S. Analysis on the geologic conditions and the assessment of the further ore-finding foreground from Dahutang to Liyangdou metallogenic region in the western part of the Jiulingshan, Jiangxi Province. *Resour. Environ. Eng.* **2006**, *20*, 348–353. (In Chinese)
32. Zhong, Y.F.; Ma, C.Q.; She, Z.B.; Lin, G.C.; Xu, H.J.; Wang, R.J.; Yang, K.G.; Liu, Q. SHRIMP U-Pb zircon geochronology of the Jiuling granitic complex batholith in Jiangxi province. *Earth Sci.* **2005**, *30*, 685–691. (In Chinese)
33. Sun, K.K.; Chen, B.; Chen, J.S.; Xiang, X.K. The petrogenesis of the Jiuling granodiorite from the Dahutang deposit, Jiangxi Province and its tectonic implications. *Acta Petrol. Sin.* **2017**, *33*, 907–924. (In Chinese)
34. Zhang, Z.H. Research on Mineralization of the Dahutang Tungsten Multimetal Field, Jiangxi Province, China. Ph.D. Thesis, China University of Geosciences, Beijing, China, 2014; pp. 1–148. (In Chinese).
35. Huang, L.C. Geochemistry of Mesozoic Magmatic Evolutions and Mineralizations in the Giant Dahutang Tungsten Deposit, Northern Jiangxi Province, China. Ph.D. Thesis, Nanjing University, Nanjing, China, 2014; pp. 1–129. (In Chinese).
36. Zhu, L.M.; Zhang, G.W.; Li, B.; Guo, B.; Kang, L.; Lv, S.L. Geology, isotope geochemistry and ore genesis of the Maanqiao gold deposit, Shanxi Province. *Acta Petrol. Sin.* **2009**, *25*, 431–443. (In Chinese)
37. Yang, X.; Liu, J.J.; Han, S.Y.; Jiang, H.; Zhai, D.G.; Liu, Y.D.; Luo, C. S-Pb-H-O isotopic characteristics of the Luchun Cu-Pb-Zn deposit, Deqin County, Yunnan, and geological implications. *Geochimica* **2012**, *41*, 240–249. (In Chinese)
38. Sun, S.S.; McDonough, W.F. Chemical and isotopic systematics of oceanic basalts: Implications for mantle composition and processes. *Geol. Soc. Lond. Spec. Publ.* **1989**, *42*, 313–345. [[CrossRef](#)]
39. Wesolowski, D.; Ohmoto, H. Oxygen isotope fractionation in the minerals scheelite and powellite from theoretical calculation. *Econ. Geol.* **1983**, *64*, 334.
40. Nassau, K.; Loiacono, G.M. Calcium tungstate—III: Trivalent rare earth substitution. *J. Phys. Chem. Solids* **1963**, *24*, 1503–1510. [[CrossRef](#)]
41. Burt, D.M. Compositional and phase relations among rare earth elements. *Rev. Mineral.* **1989**, *21*, 259–307.
42. Ghaderi, M.; Palin, J.M.; Campbell, I.H.; Sylvester, P.J. Rare earth element systematics in scheelite from hydrothermal gold deposits in the Kalgoorlie-Norseman region, Western Australia. *Econ. Geol.* **1999**, *94*, 423–437. [[CrossRef](#)]
43. Brugger, J.; Lahaye, Y.; Costa, S.; Lambert, D.; Bateman, R. Inhomogeneous distribution of REE in scheelite and dynamics of Archaean hydrothermal systems (Mt. Charlotte and Drysdale gold deposits, Western Australia). *Mineral. Petrol.* **2000**, *139*, 251–264. [[CrossRef](#)]
44. Peng, J.T.; Hu, R.Z.; Zhao, J.H.; Fu, Y.Z.; Yuan, S.D. Rare earth element (REE) geochemistry for scheelite from the Woxi Au-Sb-W deposit, western Hunan. *Geochimica* **2005**, *34*, 115–122. (In Chinese)
45. Xiong, D.X.; Sun, X.M.; Shi, G.Y.; Wang, S.W.; Gao, J.F.; Xue, T. Trace elements, rare earth elements (REE) and Nd-Sr isotopic compositions in scheelites and their implications for the mineralization in Daping gold mine in Yunnan Province, China. *Acta Petrol. Sin.* **2006**, *22*, 733–741. (In Chinese)
46. Ye, L.; Bao, T.; Liu, Y.P.; He, F.; Wang, X.J.; Zhang, Q.; Wang, D.P.; Lan, J.B. The trace and rare earth elements in scheelites and their implication for the mineralization in Dulong Sn-Zn polymetal ore deposit, Yunnan Province. *J. Nanjing Univ. Nat. Sci.* **2018**, *54*, 31–44. (In Chinese)
47. Zhao, W.; Zhou, M.F.; Williams-Jones, A.E.; Zhao, Z. Constraints on the uptake of REE by scheelite in the Baoshan tungsten skarn deposit, South China. *Chem. Geol.* **2018**, *477*, 123–136. [[CrossRef](#)]
48. Ye, Z.H.; Wang, P.; Li, Y. Mineralization in the Shimensi Deposit, Northern Jiangxi Province, China: Evidence from Pb and O isotopes. *Geochim. J.* **2021**, *55*, 39–49. [[CrossRef](#)]
49. Hsu, L.C.; Galli, P.E. Origin of the scheelite-powellite series of minerals. *Econ. Geol.* **1973**, *68*, 681–696. [[CrossRef](#)]
50. Rempel, K.U.; Williams-Jones, A.E.; Migdisov, A.A. The partitioning of molybdenum (VI) between aqueous liquid and vapor at temperatures up to 370 °C. *Geochim. Cosmochim. Acta* **2009**, *73*, 3381–3392. [[CrossRef](#)]
51. Song, G.X.; Qin, K.Z.; Li, G.M.; Evans, N.J.; Chen, L. Scheelite elemental and isotopic signatures: Implications for the genesis of skarn-type W-Mo deposits in the Chizhou area, Anhui Province, eastern China. *Am. Mineral.* **2014**, *99*, 303–317. [[CrossRef](#)]
52. Bau, M.; Moeller, P. Rare earth element fractionation in metamorphogenic hydrothermal calcite, magnesite and siderite. *Mineral. Petrol.* **1992**, *45*, 231–246. [[CrossRef](#)]
53. Bau, M.; Dulski, P. Comparative study of yttrium and rareearth behaviors in fluorine-rich hydrothermal fluids. *Contrib. Mineral. Petrol.* **1995**, *119*, 213–223. [[CrossRef](#)]
54. Zhang, L.G. Lead isotopic compositions of feldspar and ore and their geologic significance. *Miner. Depos.* **1988**, *7*, 55–64. (In Chinese)
55. Dickin, A.P. *Radiogenic Isotope Geology*, 2nd ed.; Cambridge University Press: Cambridge, UK, 2005; pp. 101–135.
56. Chen, D.G.; Zhi, H.X.; Yang, H.T. *Geochemistry*; University of Science and Technology of China Press: Hefei, China, 2009; p. 4499. (In Chinese)
57. Ma, Z.D.; Shan, G.X. The background of regional lead isotopic compositions and its application in the Lower and Middle Reaches of the Yangtze River and Neighbouring area. *Acta Geol. Sin.* **1996**, *70*, 324–334. (In Chinese)
58. Barnes, H.L. *Geochemistry of Hydrothermal Ore Deposit*; Wiley: New York, NY, USA, 1979.